INTERNATIONAL JOURNAL FOR NUMERICAL METHODS IN FLUIDS, VOL. 23, 379–396 (1996)

THREE-DIMENSIONAL VISCOUS FLOW THROUGH A ROTATING CHANNEL: A PSEUDOSPECTRAL MATRIX METHOD APPROACH

H. B. CHEN

Advanced Laser and Fusion Technology, Inc., 189 Deveault St., Unit 7, Hull, Que. J8Z 1S7, Canada

K. NANDAKUMAR AND W. H. FINLAY

Faculty of Engineering, University of Alberta, Edmonton, Alba. T6G 2G8, Canada

H. C. KU

Applied Physics Laboratory, The Johns Hopkins University, Laurel, MD 20707, U.S.A

SUMMARY

A Fourier–Chebyshev pseudospectral method is used for the numerical simulation of incompressible flows in a three-dimensional channel of square cross-section with rotation. Realistic, non-periodic boundary conditions that impose no-slip conditions in two directions (spanwise and vertical directions) are used. The Navier–Stokes equations are integrated in time using a fractional step method. The Poisson equations for pressure and the Helmholtz equation for velocity are solved using a matrix diagonalization (eigenfunction decomposition) method, through which we are able to reduce a three-dimensional matrix problem to a simple algebraic vector equation. This results in signficant savings in computer storage requirement, particularly for large-scale computations. Verification of the numerical algorithm and code is carried out by comparing with a limiting case of an exact steady state solution for a one-dimensional channel flow and also with a two-dimensional rotating channel case. Two-cell and four-cell two-dimensional flow patterns are observed in the numerical experiment. It is found that the four-cell flow pattern is stable to symmetrical disturbances but unstable to asymmetrical disturbances.

KEY WORDS: rotating flow; three-dimensional rectangular channel; pseudospectral matrix method; eigenvalue decomposition; two- and four-cell flow pattern

1. INTRODUCTION

The study of flow through a rotating rectangular channel is of theoretical and practical importance. Practically, rotating channel flow is common in rotating machines, such as coolant flow within turbine blades, pulp flow in paper refiners, flow in centrifugal pumps and in instruments that measure mass flow based on the Coriolis effect. On the other hand, the theoretical study of rotating flow can lead to a better understanding of secondary flow motion, bifurcations, secondary stability and the transition to turbulence. As the flow undergoes rather complex structural changes, it provides a useful framework for testing computational algorithms to see whether they can capture all the nuances exhibited by the flow. This requires verification with either experiments or cross validation using different computational discretization schemes.

CCC 0271-2091/96/040379-18

Received May 1995
Revised November 1995

Existing studies on rotating channel flows are limited eitehr to two-dimensional fully developed flow[1,2] or, in the three-dimensional case, to an idealized infinite geometry subjected to spanwise periodic boundary conditions.[3] In this study we present a three-dimensional, time-dependent numerical algorithm for studying the flow in a rotating channel with realistic, no-slip boundary conditions in both the vertical and spanwise directions. Since the flow is pressure-driven in the streamwise (x-) direction, we look for solutions that have no streamwise variation (two-dimensional solutions) as well as those that break the translated invariance in the x-direction, resulting in streamwise periodic (three-dimensional) solutions. To allow for these effects, periodicity is imposed in the streamwise direction only. Since time variation is also allowed in the formulation, we should be able to capture any travelling wave solutions also. The present formulation will not capture spatially evolving flows in the streamwise direction because of the use of periodic conditions in that direction.

In certain areas of computational fluid dynamics, especially in the study of the mechanism of early transition to turbulence, spectral methods have been used quite successfully.[4–7] For three-dimensional channel computations, most existing methods and codes are based on the assumption of periodic boundary conditions in two directions (streamwise and spanwise), which is useful for investigating homogeneous turbulence. In several recent studies the periodic boundary condition has been replaced with no-slip conditions for duct flow, which might reveal the physics of wall turbulence by direct numerical simulation. This of course requires that the algorithm be reliable and such an algorithm should be its limiting cases capture all the known lower-dimensional flow features such as multiplicity and stability of simpler flows. Such algorithms have not been tested from such a perspective and this is the main motivation for the present work. In other words, the question that we pursue is: can a single algorithm, that has all the degrees of freedom in all three spatial and temporal directions and very little assumption concerning symmetries in the flow, capture the entire range of structural changes in flow behaviour over the entire parameter range? This is obviously a formidable task. Our attempt is a modest one of assembling such a code from existing knowledge of various aspects of the numerical scheme and validating it against certain known bifurcation phenomena of two-dimensional solutions and their stability. The temporal formulation provides a natural medium for testing the stability aspects as well.

The governing equations are given in Section 2. The numerical methods are described in Section 3. Finally, results that validate the present algorithm are discussed in Section 4.

2. GOVERNING EQUATIONS

The governing equations are the incompressible, Navier–Stokes equations in a reference frame that rotates with the channel:

$$\frac{\partial \mathbf{v}^*}{\partial t^*} + (\mathbf{v}^* \cdot \nabla^*)\mathbf{v}^* + 2\vec{\omega} \times \mathbf{v}^* = -\nabla^*\varphi + \nu\Delta^*\mathbf{v}^*, \tag{1}$$

$$\nabla^* \cdot \mathbf{v} = 0, \tag{2}$$

where an asterisk indicates a dimensional quantity. Here $\mathbf{v}^* = (u^*, v^*, w^*)$ represents the velocity fields, φ is a potential that combines the thermodynamic pressure with centrifugal and gravitational terms, $\vec{\omega}$ is the rotation vector, with $\vec{\omega} = (0, \Omega, 0)$ and v is the kinematic viscosity.

Using the dimensionless variables

$$\mathbf{v} = \frac{\mathbf{v}^*}{U}, \qquad x = \frac{x^*}{L}, \qquad y = \frac{y^*}{h}, \qquad z = \frac{z^*}{b}, \qquad \tau = t^*\Omega, \tag{3}$$

where $\mathbf{v} = (u, v, w)$, $U = -(\partial\varphi/\partial x)/\rho\Omega$ and L, h and b are the dimensional lengths of the channel in the $x-, y-$ and z-direction respectively, equation (1) can be written as

$$\frac{\partial u}{\partial t} + Ro\left(\gamma_x u\frac{\partial u}{\partial x} + \gamma_y v\frac{\partial u}{\partial y} + w\frac{\partial u}{\partial z}\right) + 2w = 1 - \frac{\partial p}{\partial x} + Ek\left(\gamma_x^2\frac{\partial^2 u}{\gamma x^2} + \gamma_y^2\frac{\partial^2 u}{\partial y^2} + \frac{\partial^2 u}{\partial z^2}\right), \tag{4}$$

$$\frac{\partial v}{\partial t} + Ro\left(\gamma_x u\frac{\partial v}{\partial x} + \gamma_y v\frac{\partial v}{\partial y} + w\frac{\partial v}{\partial z}\right) = -\frac{\partial p}{\partial y} + Ek\left(\gamma_x^2\frac{\partial^2 v}{\partial x^2} + \gamma_y^2\frac{\partial^2 v}{\partial y^2} + \frac{\partial^2 v}{\partial z^2}\right), \tag{5}$$

$$\frac{\partial w}{\partial t} + Ro\left(\gamma_x u\frac{\partial w}{\partial x} + \gamma_y v\frac{\partial w}{\partial y} + w\frac{\partial w}{\partial z}\right) - 2u = -\frac{\partial p}{\partial z} + Ek\left(\gamma_x^2\frac{\partial^2 w}{\partial x^2} + \gamma_y^2\frac{\partial^2 w}{\partial y^2} + \frac{\partial^2 v}{\partial z^2}\right). \tag{6}$$

Here $Ro = U/b\Omega$ is the Rossby number, representing the ratio of convective inertial force to Coriolis force, $Ek = v/b^2\Omega$ is the Ekman number, representing the ratio of viscous force to Coriolis force, and $\gamma_x = b/L$ and $\gamma_y = b/h$ are the aspect ratios in the x- and y-direction respectively. The pressure in the streamwise direction has been decomposed into a mean pressure gradient (which is used as a scale in U) which drives the primary flow in the streamwise direction.

The boundary conditions are (Figure 1) (a) periodic in the x-direction,

$$\mathbf{v}(0, y, z, t) = \mathbf{v}(2\pi, y, z, t),$$

(b) no slip at the walls in the y- (vertical) direction,

$$\mathbf{v}(x, 0, z, t) = \mathbf{v}(x, 1, z, t) = 0,$$

and (c) no-slip at the walls in the z- (spanwise) direction,

$$\mathbf{v}(x, y, 0, t) = \mathbf{v}(x, y, 1, t) = 0.$$

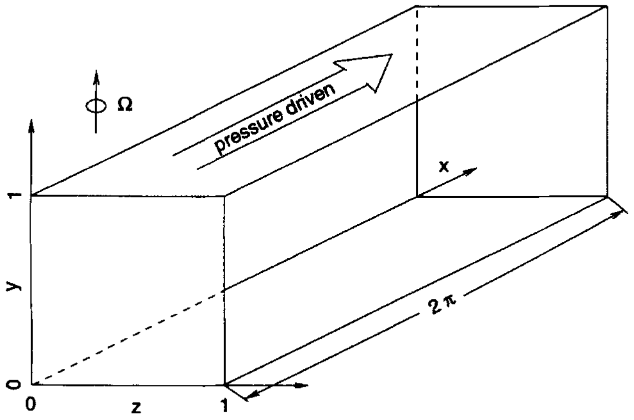

Figure 1. Flow in a 3D rotating channel

3. NUMERICAL METHOD

The numerical algorithm used here is not entirely new. Eigenvalue decomposition and fractional step methods have been discussed well in the literature.[4,7] Application of the scheme to a realistic and experimentally realizable flow condition makes it suitable for validation of such a scheme. The validation in the present work is achieved by comparing with previously known solutions computed using entirely different numerical schemes.

In the present work, Chebyshev polynomials that satisfy the no-slip condition on the duct boundaries are used. Periodic boundary conditions are used only in the streamwise direction. Time evolution is tracked with the fractional step method. We have focused on the lower range of the parameter space where multiplicity and stability features of the flows are known from other independent, two-dimensional studies. Reliable calculation of flows at higher flow conditions leading to turbulent flows is not attempted here. It will be the subject of future work.

3.1. *Spatial discretization*

Here is a brief description of the Fourier–Chebyshev matrix method adopted from References 5 and 7. In the streamwise direction a Fourier series is used as the basis functions and the collocation points are selected as

$$x_i = \frac{2\pi i}{N_x}, \quad i = 0, 1, \ldots, N_x - 1.$$

The spatial derivatives are given by

$$\frac{\mathrm{d}^p u(x_i)}{\mathrm{d}x^p} = \sum_{k=0}^{N-1} d^p_{i,k} u_k, \quad p = 1, 2,$$

where p represents the first and second derivatives and $d^p_{i,k}$ are the spatial derivative matrices whose elements are given in References 4 and 6.

For the vertical and spanwise directions, Chebyshev polynomials are used as the basis functions and the collocation points are selected as

$$y_j = \frac{1}{2}\left[1 + \cos\left(\frac{\pi(j-1)}{N_y}\right)\right], \quad j = 1, \ldots, N_y + 1,$$

$$z_i = \frac{1}{2}\left[1 + \cos\left(\frac{\pi(k-1)}{N_z}\right)\right], \quad k = 1, \ldots, N_z + 1.$$

The spatial derivatives based on the Chebyshev basis functions are given by

$$\frac{\mathrm{d}^p u(y_j)}{\mathrm{d}y^p} = \sum_{l=1}^{N_y+1} G^p_{j,l} u_l, \quad p = 1, 2, \qquad \frac{\mathrm{d}^p u(z_k)}{\mathrm{d}z^p} = \sum_{l=1}^{N_z+1} G^p_{k,l} u_l, \quad p = 1, 2,$$

where p represents the first and second derivatives and $G^p_{j,l}$ are given in References 4 and 6.

3.2. *Temporal discretization*

The governing equations (4)–(6) can be written in index form as

$$\frac{\partial u_i}{\partial t} + Ro\, u_j \frac{u_i}{\partial x_j} + 2\varepsilon_{ijk} u_j \Omega_k = -\frac{\partial p}{\partial x_i} + Ek \frac{\partial^2 u_i}{\partial x_j^2}. \tag{7}$$

A fractional step method is used for temporal discretization and advancement as follows.

First fractional step. The non-linear terms and Coriolis terms are advanced explicitly from n to $n+\frac{1}{3}$ using the RK3 (a low-storage version of third-order Runge–Kutta[4] method in the form

$$u_i^{n+1/3} = u_i^n + \left(Ro\, u_j \frac{\partial u_i}{\partial x_j} + 2\varepsilon_{ijk} u_k \Omega_k \right)_{\mathrm{RK3}}^n . \tag{8}$$

The Courant number for this explicit method is

$$CFL = \max\left\{ \left|\frac{u}{\Delta x}\right| + \left|\frac{v}{|\Delta y(y)|}\right| + \left|\frac{w}{|\Delta z(z)|}\right| \right\} \Delta t. \tag{9}$$

The directions y and z have non-periodic boundary conditions and non-uniform Δy and Δz are used.

Second fractional step. The viscous terms are advanced implicitly from $n+\frac{1}{3}$ to $n+\frac{2}{3}$ using the Crank–Nicolson method in the form

$$u_i^{n+2/3} = u_i^{n+1/3} + \frac{\Delta t Ek}{2} (\nabla^2 u_i^{n+1/3} + \nabla^2 u_i^{n+2/3}). \tag{10}$$

After simple algebraic manipulation we end up solving the Helmholtz equation for velocity in this step:

$$\nabla^2 u_i^{n+2/3} - \lambda u_i^{n+2/3} = -(\nabla^2 u_i^{n+1/3} - \lambda u_i^{n+1/3}), \tag{11}$$

where $\lambda = 2/\Delta t Ek$.

Third fractional step. Pressure correction is applied at the last step so that

$$u_i^{n+1} = u_i^{n+2/3} - \Delta t \nabla p^{n+1}, \tag{12}$$

with the divergence-free condition enforced as

$$\frac{\partial u_i^{n+1}}{\partial x_i} = 0. \tag{13}$$

Therefore we have a Poisson equation for the pressure:

$$\nabla^2 p^{n+1} = \frac{1}{\Delta t} \nabla \cdot u^{n+2/3}. \tag{14}$$

Thus the divergence-free condition is satisfied at the end of each full step.

3.3. Eigenvalue decomposition method for Helmholtz equation and Poisson equation

With the fractional step method (splitting technique) mentioned above, we must solve a Helmholtz equation for velocity at the second fractional step and a Poisson equation for pressure at the last fractional step. For three-dimensional unsteady flow this causes difficulties in both storage and speed of computation. To overcome these difficulties, an eigenvalue decomposition method is used to deal with the Helmholtz equation and the Poisson equation.

Similar to the Schur decomposition, the eigenvalue decomposition method, also called matrix diagonalization, has come to be known as the Haidvogel–Zang algorithm in fluid dynamics after the paper by Haidvogel and Zang.[8] Here we briefly give the procedure of the eigenvalue decomposition (matrix diagonlization) method for solving the Helmholtz equation.

For the sake of simplicity, equation (11) can be written as a standard form of the Helmholtz equation (one-component velocity):

$$D_x^2 u + D_y^2 u + D_z^2 u - \lambda u = S, \tag{15}$$

where D_x^2, D_y^2 and D_z^2 are the second-derivative operators and S is the source term representing the right side of (11). Generalizing to three components of velocity is straightforward. Equation (15) can be decomposed into eigenspace as

$$(\alpha_i + \beta_j + \gamma_k)\hat{u} - \lambda\hat{u} = \hat{S}, \tag{16}$$

where α_i, β_j and γ_k are the eigenvalues of the operators D_x^2, D_y^2 and D_z^2 respectively given by

$$\{\alpha_1 \cdots \alpha_i \cdots \alpha_{N_x}\} = \mathbf{EX}^{-1}D_x^2\mathbf{EX},$$
$$\{\beta_1 \cdots \beta_j \cdots \beta_{N_y}\} = \mathbf{EY}^{-1}D_y^2\mathbf{EY},$$
$$\{\gamma_1 \cdots \gamma_k \cdots \gamma_{N_z}\} = \mathbf{EZ}^{-1}D_z^2\mathbf{EZ}.$$

Here **EX**, **EY** and **EZ** are the eigenvectors of the operators D_x^2, D_y^2 and D_z^2 respectively and $\hat{u}$ and $\hat{S}$ represent u and S in eigenspace respectively. After decomposition for each i, j, k the Helmholtz equation becomes a simple algebraic equation (16) in eigenspace, which can be solved with simple algebra immediately as

$$\hat{u} = \frac{\hat{S}}{\alpha_i + \beta_j + \gamma_k - \lambda}, \tag{17}$$

where

$$\hat{S} = \mathbf{EX}^{-1}S(\mathbf{EY}^{\mathrm{T}})^{-1}(\mathbf{EZ}^{\mathrm{T}})^{-1}.$$

The value of u can be obtained in physical space by the matrix multiplication

$$u = \mathbf{EX}\,\hat{u}\,\mathbf{EY}^{\mathrm{T}}\mathbf{EZ}^{\mathrm{T}}. \tag{18}$$

A similar procedure can be used for solving the Poisson equation. Ku *et al.*[7] give an implementation for the pressure Poisson equation in detail, especially in dealing with the boundary conditions. This method can reduce storage from $N^3 \times N^3$ to N^3 in both the Helmholtz equation and the Poisson equation. Since operators such as eigenvalues and eigenvectors are invariant in time, they can be computed at the first step, saved and used subsequently for each time step computation. For three-dimensional unsteady problems this method is advantageous over the 3D direct inverse method in both storage and time. (One also has to be careful to deal with the corner singularity in the 3D direct inverse method.)

4. RESULTS AND DISCUSSION

Extensive tests were carried out to select suitable time and spatial discretization parameters that yielded grid-independent results. The time step was chosen not only to meet, the *CFL* condition but also to control the truncation error. For all one- and two-dimensional solutions a spatial resolution of $3 \times 15 \times 15$ was used in the calculation, which was deemed adequate since increasing the resolution did not affect the results significantly.

4.1. Rectilinear flow ($Ek \to \infty$)

The above-described algorithm and code for rotating channel flow can be verified with rectilinear flow ($EK \to \infty$), for which there is an analytical solution, and also compared with existing 2D results.

There are two asymptotic limit cases for rotating channel flow. When the channel rotates slowly, the flow is the slow rotation limit of creeping rectilinear flow ($EK \to \infty$) where viscous forces are dominant. When the channel rotates rapidly, the flow is the rapid rotation limit of Ekman boundary layer flow ($EK \to 0$) where the Coriolis force plays the dominant role. For the slow rotation limit case ($Ek \to \infty, Ro = 0$) with $\gamma_y = 1$ the governing equation (4) reduces to the Poisson equation

$$Ek\left(\frac{\partial^2 u}{\partial y^2}+\frac{\partial^2 u}{\partial z_2}\right) = -1. \tag{19}$$

An exact solution obtained using the separation-of-variables method[1] for velocity is

$$u = \frac{1}{Ek}\sum_{m=0}^{\infty}\sum_{n=0}^{\infty}\frac{16\sin[(2n+1)\pi z]\sin[(2m+1)\pi y]}{\pi^4(2n+1)(2m+1)[(2n+1)^2+(2m+1)^2]}.$$

The total volumetric flux along the channel for this rectilinear flow case (Ek being unity) is

$$Q = \int_0^1\int_0^1 u\,\mathrm{d}y\,\mathrm{d}z = 0{\cdot}0348.$$

To compare with the exact solution, a computation was carried out for a limiting case with $Ek \to \infty$ and $Ro = 0$. The computation was carried out on an SGI Iris R3000A with 32 Mbytes RAM. The CPU time required for impulsively started flow to reach steady state was about 70 h. Figure 2 shows the flow rate as a function of dimensionless time. At $t = 0{\cdot}3$ the flow has reached a steady state with flow rate $Q = 0{\cdot}0350906$, whereas the exact flow rate is $Q = 0{\cdot}0348$ for the duct with the domain of cross-section being $y \in [0, 1], z \in [0, 1]$. (The exact flow rate for a duct with the domain of cross-section being $y \in [-1, 1], z \in [-1, 1]$ is $Q = 0{\cdot}56227$ and our code gives $Q = 0{\cdot}5684$.) This is a global test for the algorithm and code, yet it is a crucial one, since the result is obtained by solving the complete equations (4)–(6) with $Ek = 1$ and $Ro = 0$ instead of solving the Poisson equation. It tests the capability of the asymptotic limits of the code. As shown in Figure 2 agreement is quite satisfactory. Figure 3(a) shows the contour plot of the axial (streamwise) velocity over a cross-section of the duct. Figure 3(b)

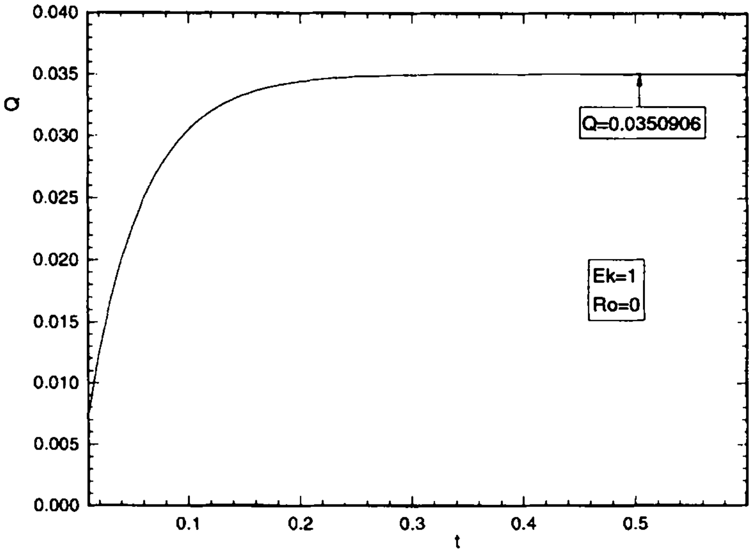

Figure 2. Rectilinear flow case: flow rate versus time

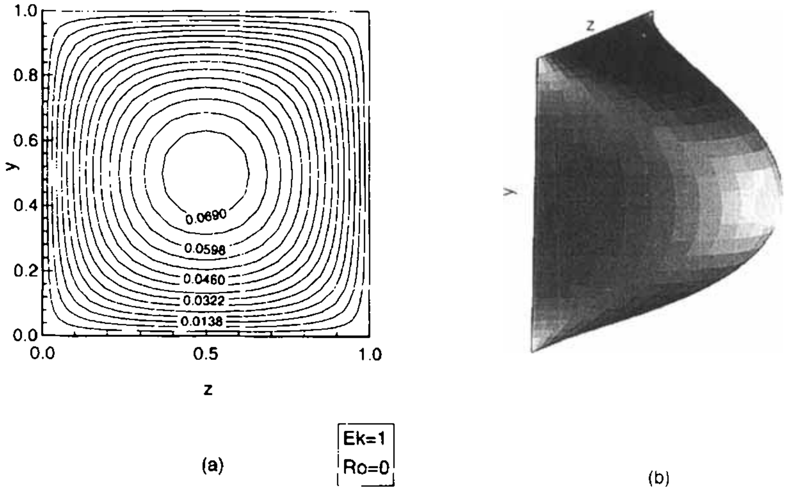

Figure 3. Rectilinear flow cases: (a) contour plot of axial velocity. (b) spatial view of axial velocity profile

shows the perspective plot of the axial velocity as a function of y and z. In the slow rotation limit of rectilinear flow the streamwise velocity profile along the height and width of the channel is a parabolic, Poiseuille-type velocity profile. Observe the reflective symmetry about both the y and z-axis in Figure 3. Of course, the flow reaches a time-invariant state as shown in Figure 2 and there is no streamwise variation of the flow. Thus, although all the degrees of freedom in the space and time domain were allowed in the model, the simulation converges to a one-dimensional, steady flow, since there is a stable solution with these attributes in this parameter region.

4.2. *Two-cell structures ($Ek = 0{\cdot}01$, $Ro = 0$, $Ro = 1$)*

It is well known that in channels of finite extent in the y- and z-direction a secondary flow, driven by Coriolis force, begins to develop in the cross-plane (y, z) even for a small rate of rotation. The common secondary flow pattern is a two-cell flow pattern with reflective symmetry along the middle of the channel perpendicular to the axis of rotation (i.e. ($y = 0{\cdot}5, z$)). Observe that the reflective symmetry of the one-dimensional solution about the ($y, z = 0{\cdot}5$) axis is broken by the system rotation. Computations for Ekman number $Ek = 0{\cdot}01$ and Rossby numbers $Ro = 0$ and $Ro = 1$, where both viscous and Coriolis forces are important, are performed using our 3D code. However, the converged steady state results show no streamwise variation, because there are stable two-dimensional solutions in this region of the parameter space. Figure 4 shows the flow rate as a function of time for $Ek = 0{\cdot}01$ and $Ro = 0$. The flow has reached a steady state with flow rate $Q = 2{\cdot}47018$. Figure 5(a) shows the contour plot of the axial (streamwise) velocity and Figure 5(b) shows the perspective plot of the axial velocity profile at $Ek = 0{\cdot}01$ and $Ro = 0$. When we increase the rotation rate, the maximum velocity along the y-axis starts to shrink owing to the appearance of the secondary flow in the cross-section (two-cell flow pattern in Figure 5(c)). As the rotation rate increases to $Ek = 0{\cdot}01$, the so-called Taylor–Proudman configuration in the interior of the channel appears.

Figure 6 shows the flow rate as a function of time with $Ek = 0{\cdot}01$ and $Ro = 1$. The flow has reached a steady state with flow rate $Q = 2{\cdot}1943$, lower than the value $Q = 2{\cdot}47018$ computed at $Ro = 0$. This is because of the intensification of the secondary flow with increasing Rossby number, resulting in a decreased flow rate at a fixed imposed streamwise pressure gradient. The contour plot and perspective

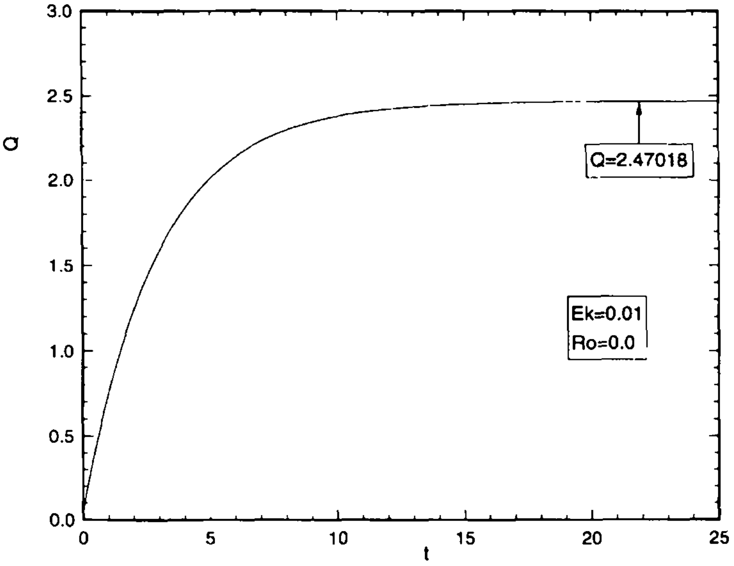

Figure 4. Flow rate versus time

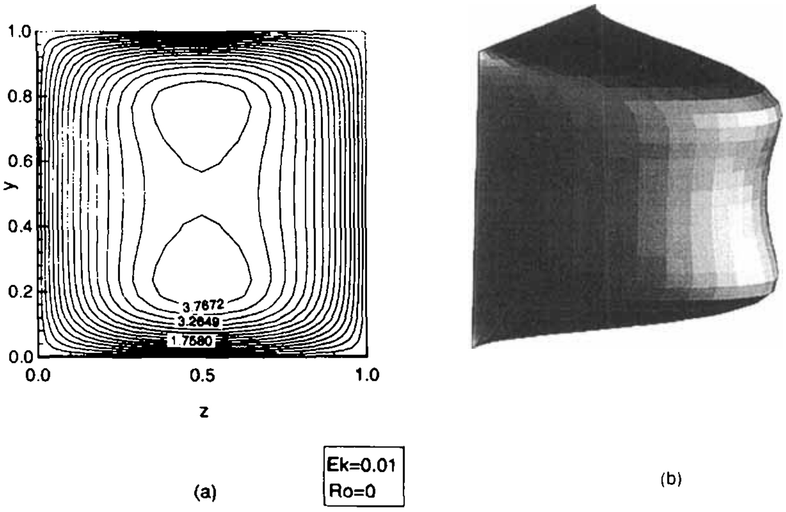

(a) (b)

Figure 5. (a) Contour plot of axial velocity. (b) Spatial view of axial velocity profile

plot of the axial velocity profile are shown in Figure 7. The Taylor–Proudman configuration is demonstrated clearly in Figure 7(b). The streamwise velocity is nearly flat in the interior of the channel in Figure 7(b), while near the upper and lower floors of the channel an Ekman layer begins to develop. Figures 7(a) and 7(b) show the two regions clearly: the interiorr geostrophic core and the near-wall Ekman boundary layer region. In the interior region of the Taylor–Proudman column (geostrophic region) the dominant forces are the Coriolis force and the pressure force only ($2w = -\partial p/\partial x, 0 = \partial p/\partial y, 2u = \partial p/\partial z$). The outer region near the walls is the Ekman layer: the boundary layer between a geostrophic flow and the solid walls at which the no-slip condition applies. Figure 7(c) shows the secondary flow pattern as a vector plot with standard two-cell vortices at the steady state.

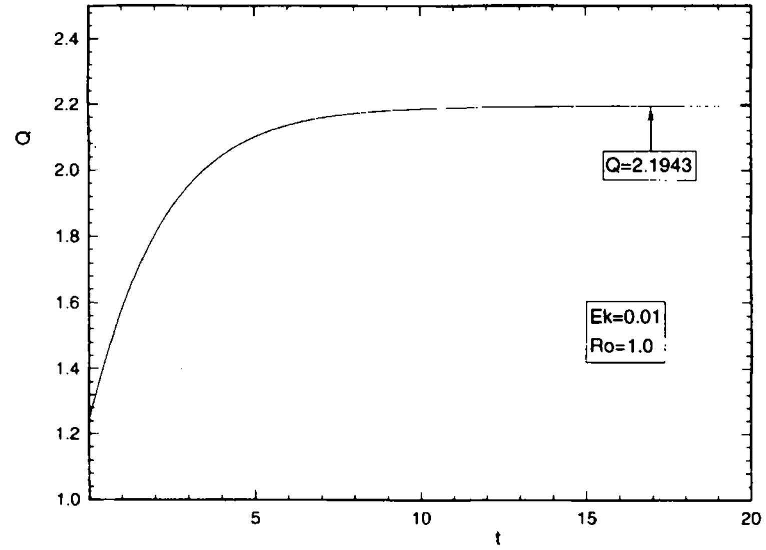

Figure 6. Flow rate versus time

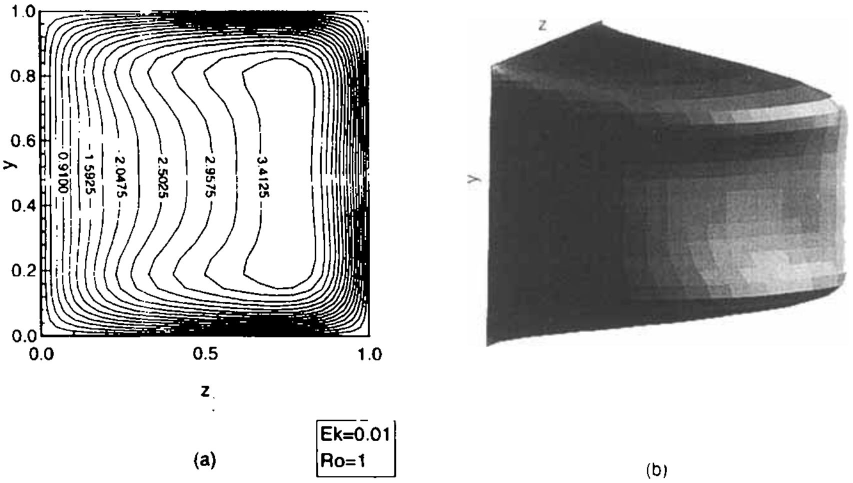

(a)

(b)

Figure 7. (a) Contour plot of axial velocity. (b) Spatial view of axial velocity profile

The two-cell flow patterns computed here are found to be axially invariant (two-dimensional). We recover such two-dimensional, steady flows in spite of using a fully three-dimensional, time-dependent code. This behaviour remains the same as we refine the grid points from 3 × 15 × 15 to 20 × 15 × 15 to let the flow vary along the axial (streamwise) direction. It is found that the two-cell pattern is indeed axially invariant. This is in excellent agreement with an existing bifurcation study of rotating channel flow[2] which shows such flows in this parameter range to be stable. It also serves as an independent check of the accuracy of the present method as against the finite difference method used in Reference 2.

4.3. *Four-cell flow pattern ($EK = 0{\cdot}01$, $Ro = 2$)*

Upon increasing the Rossby number to 2, the two-cell, two-dimensional flow was predicted to be unstable by Nandakumar *et al.*[2] In an attempt to verify that prediction by an independent simulation using the spectral method, we examine the transient evolution of the flow at $Ro = 0$.

Figure 8 shows the flow rate as a function of time with $Ek = 0{\cdot}01$ and $Ro = 2$. The flow has reached a steady state with flow rate $Q = 1{\cdot}9444$. Figure 9 shows the time evolution of the secondary flow in the cross-section of the channel. The initial condition for this transient simulation is one with a two-cell pattern found at $Ro = 1$. It is as if a two-cell state is first established by constant rotation and the speed of rotation is suddenly changed to reach a new Rossby number. Figure 9(a) shows the two-cell pattern at $t = 0{\cdot}5$ with $Ek = 0{\cdot}01$ and $Ro = 2$. By the time $t = 1{\cdot}1$ the four-cell flow pattern starts to evolve (Figure 9(b)). It is shown in Figure 9(b) that two additional small cells along the right-side wall (high-pressure wall) appear. At $t = 3$ the four-cell flow pattern is gradually formed (Figure 9(c)). The four-cell flow appears to settle down to a stable steady state (Figure 9(d)) with the saddle point located at $y = 0{\cdot}5, z = 0{\cdot}61$ (the saddle point could play a very important role in the stability of the four-cell flow pattern). The two-cell flow pattern spontaneously develops into the four-cell flow pattern with $Ek = 0{\cdot}01$ and $Ro = 2$. Figure 10(a) shows the contour plot of the axial velocity and Figures 10(b) and 10(c) show two different perspectives of the axial velocity distribution. Figures 10(b) and 10(c) show that the velocity along the z-direction is no longer symmetrical. The location of the maximum velocity shifts away from the centre of the z-direction and the maximum velocities along the y-direction occur at the top and bottom of the walls where Ekman layers are distinctive.

Figures 11 and 12 show the axial velocity profiles as functions of y and z at their centreplane $y = 0{\cdot}5, z = 0{\cdot}5$) respectively. In Figure 11 it is seen that for $Ek = 0{\cdot}01$, as the Rossby number increases (Ro = 0,1,2), the maximum axial velocities shift away from the middle plane ($z = 0{\cdot}5$) to the right wall (high-pressure wall). Owing to the Coriolis force, the maximum velocity along the z-axis direction shrinks. In Figure 12 the axial velocity distribution along the y-axis (the axis of rotation) is depicted. The Taylor–Proudman column region mentioned above is clearly demonstrated in the central region of the channel. Also, the reflective symmetry is maintained at all rotations considered.

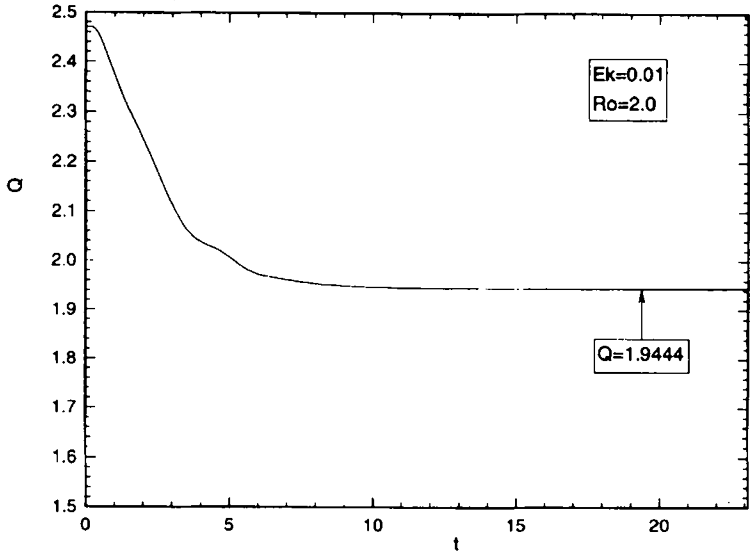

Figure 8. Flow rate versus time

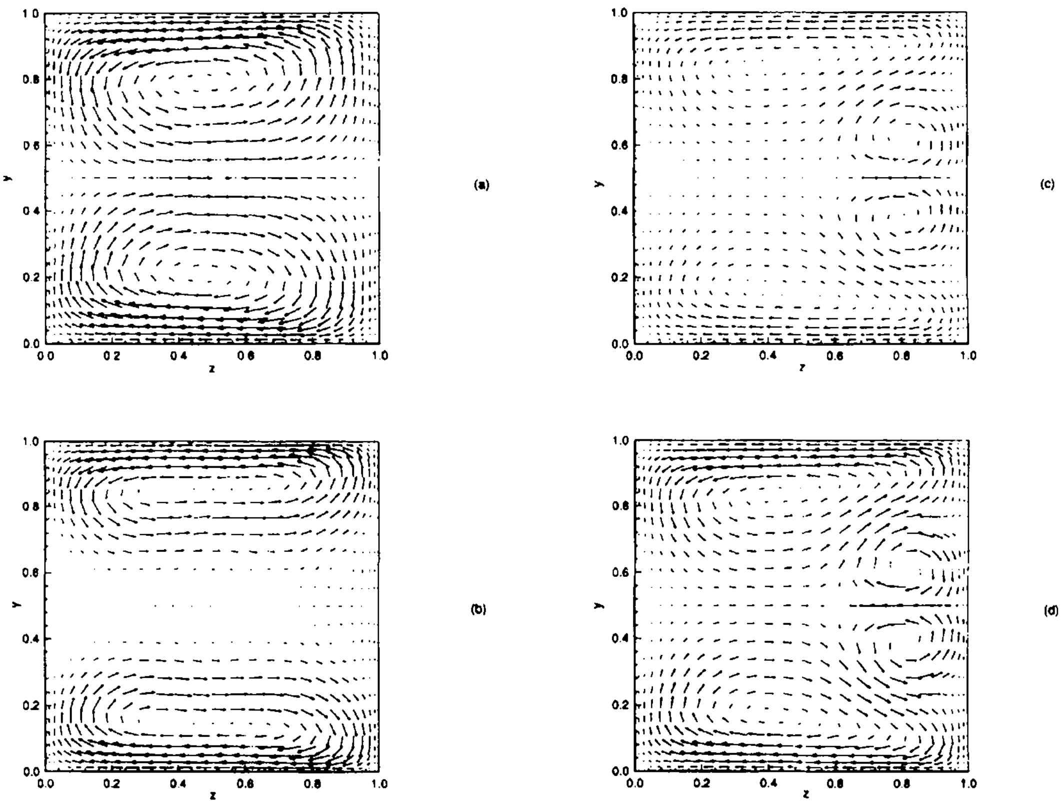

Figure 9. Vector plot of (v, w) ($Ek=0{\cdot}01$, $Ro=2$): (a) $t=0{\cdot}5$; (b) $t=1{\cdot}1$; (c) $t=3$; (d) $t=23{\cdot}1$

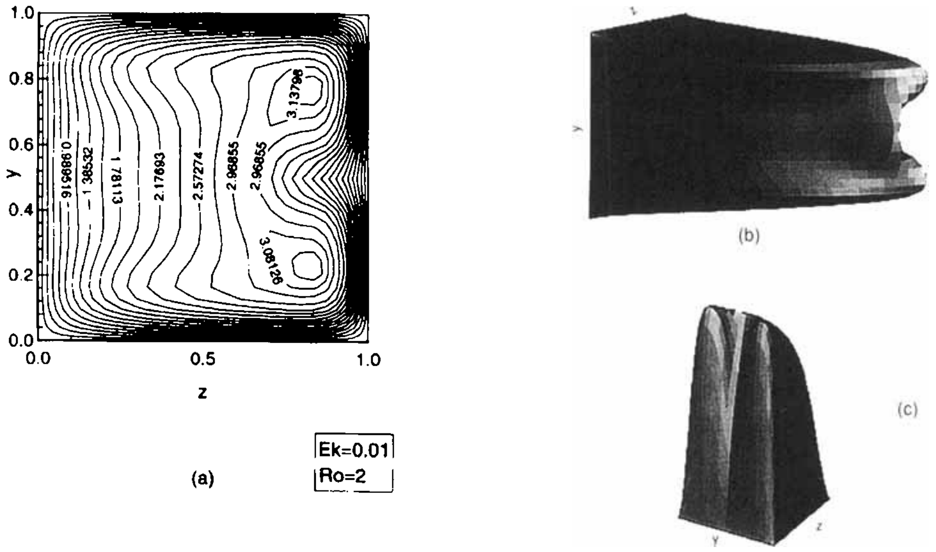

Figure 10. (a) Contour plot of axial velocity. (b) Spatial view of axial velocity profile. (c) Spatial view of axial velocity profile from different angle

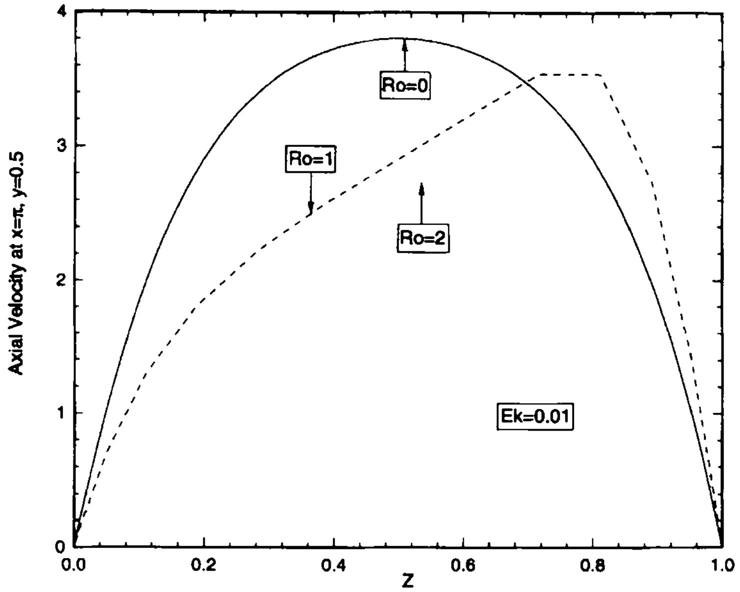

Figure 11. Velocity profile (u versus z)

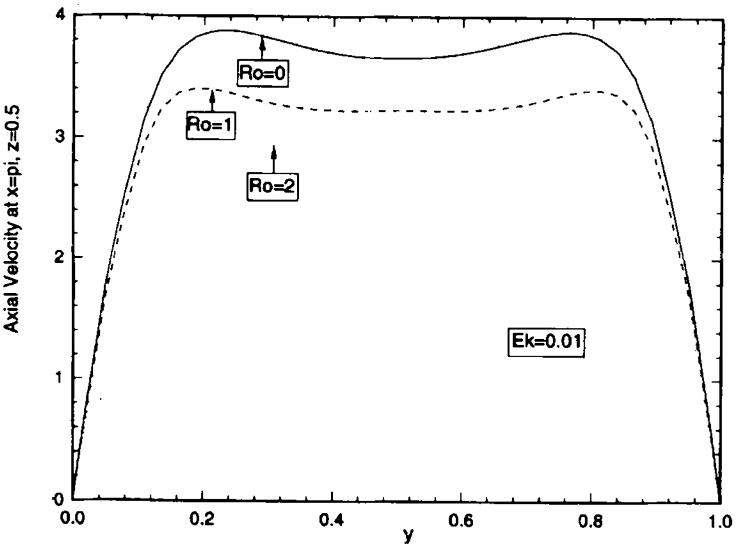

Figure 12. Velocity profile (u versus y)

In summary, we have conducted numerical simulations at $Ek = 0{\cdot}01$ with different Rossby numbers ($Ro = 0, 1, 2$) using a fully three-dimensional, transient simulation of the Navier–Stokes equations. Solutions that have a higher degree of symmetry (time invariance and streamwise invariance) are obtained in certain regions of the parameter space where such solutions are known to be stable. Two-cell flow patterns ($Ro = 0$, $Ro = 1$) and four-cell flow patterns ($Ro = 2$) have been observed. A four-cell flow pattern has developed spontaneously from a two-cell flow pattern in the present simulation. It is well known that the two-cell flow pattern is stable at low Rossby numbers. The four-cell flow pattern in rotating channel flow has been shown to be conditionally stable. In the next subsection we examine this issue.

4.4. *Stability of a four-cell flow pattern ($Ek = 0{\cdot}01$, $Ro = 2$)*

Parallel to Winter's work on the Dean problem, Nandakumar *et al.*[2] recently conducted a complete bifurcation study on the stationary, two-dimensional solutions in rotating rectangular channels. One of the main results of their work is that the four-cell, axially invariant solution is unstable to asymmetrical perturbations but stable to symmetrical perturbations. We conduct a numerical simulation using our three-dimensional code to verify this stability result.

The first step of a stability study is to identify a basic state. The basic state is the four-cell flow pattern with $Ek = 0{\cdot}01$ and $Ro = 2$. Initial symmetrical disturbances to the basic flow pattern are set up by letting all components of velocity (u, v, w) be zero at the location $y = 0{\cdot}5$, $z = 0{\cdot}5–1$. Physically this means that we put a wire or needle in the centreplane of the channel, which is the standard experimental means of perturbing the basic flow. The location of this perturbation can be seen in Figure 13 and 14.

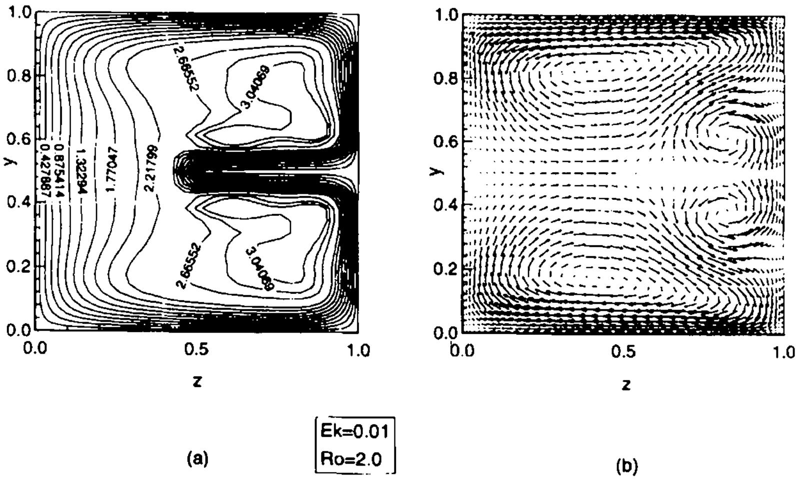

Figure 13. Symmetrial disturbances of four-cell flow pattern: (a) contour plot of u; (b) vector plot of (v, w)

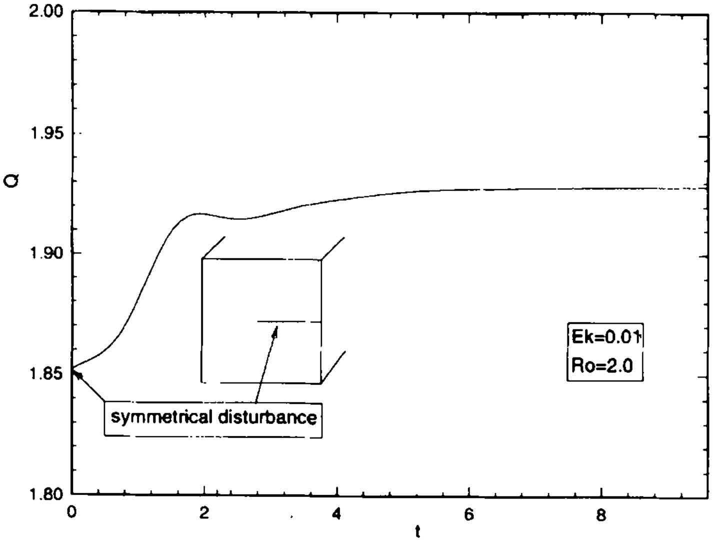

Figure 14. Flow rate versus time with symmetrical disturbances

Figure 13(a) gives the contour plot of the perturbed axial velocity and Figure 13(b) gives the vector plot of the perturbed four-cell flow pattern. Figure 14 shows the flow rate perturbed at $t = 0$ as a function of time (the inset shows the location of the initial symmetrical disturbances).

A standard hydrodynamic stability question may be asked: can this given four-cell flow pattern (physical state) withstand symmetrical disturbances and still return to its original state? The answer to this question can be found in Figure 15. Figure 15(a) shows the four-cell pattern with the above-mentioned initial symmetrical disturbances ($t = 0$). Figures 15(b)–15(d) show the flow pattern at times $t = 0{\cdot}1$, $1{\cdot}72$ and $9{\cdot}73$ respectively. They clearly show that the four-cell flow pattern goes back to its original state.

Is the four-cell flow pattern stable to asymmetrical disturbances? The answer is no. This can be demonstraed by setting up asymmetrical disturbances as shown in Figures 16 and 17. The disturbance wire or needle is now located at $y = 0{\cdot}75$, $z = 0{\cdot}5$–1. Figures 16(a) and 16(b) show the contour plot of the axial velocity and the vector plot of the secondary flow with initial asymmetrical disturbances respectively. Figure 17 shows the evolution of the flow rate when a four-cell flow is perturbed at $t = 0$ (the inset shows the location of the initial asymmetrical disturbances). The evolution of the secondary flow motion under asymmetrical disturbances can be clearly seen in Figure 18. Figure 18(a) shows the four-cell flow pattern with the above-mentioned asymmetrical disturbances ($t = 0$). Figure 18(b) shows that the two cells in the upper plane start to merge ($t = 0{\cdot}05$). As a result of the saddle point being pushed towards the high-pressure wall ($t = 0{\cdot}55$), the merged bigger cell (vortex)

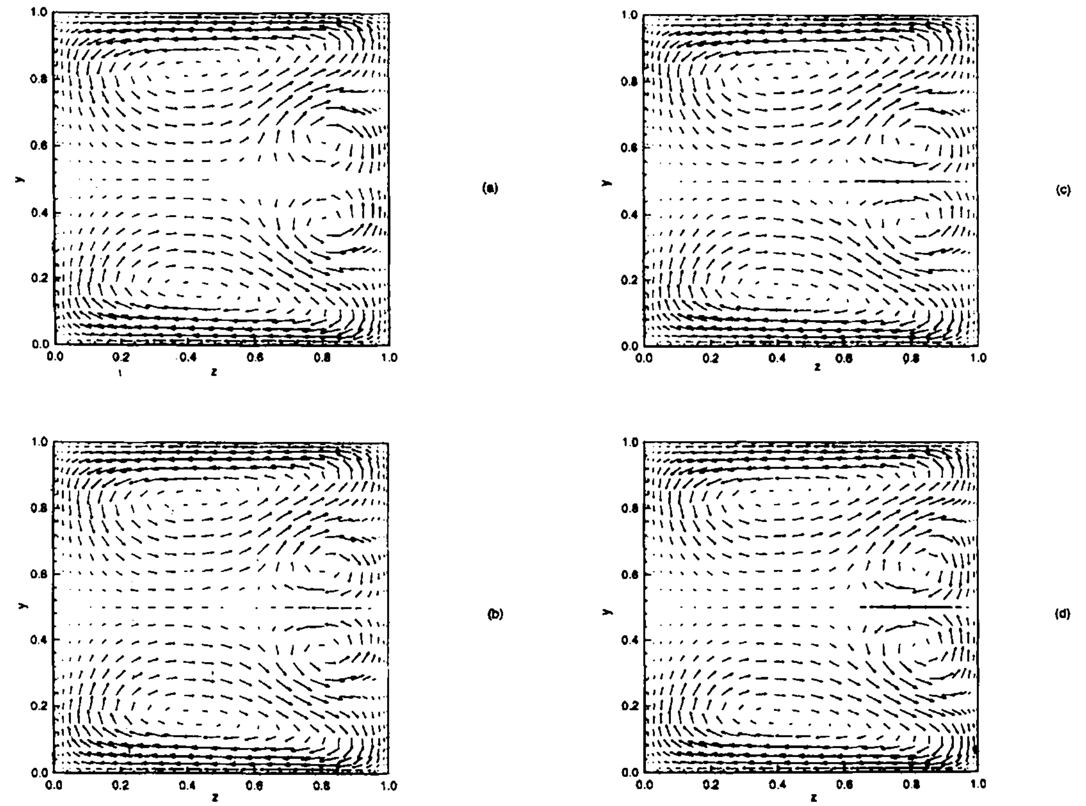

Figure 15. Vector plot of (v, w) with symmetrical disturbances ($Ek = 0{\cdot}01$, $Ro = 2$): (a) $t = 0$; (b) $t = 0{\cdot}1$; (c) $t = 1{\cdot}72$; (d) $t = 9{\cdot}73$

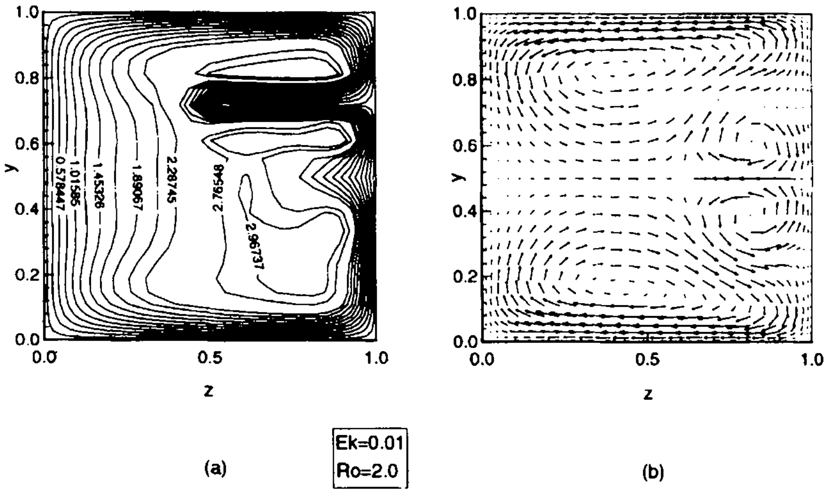

Figure 16. Asymmetrical disturbances of four-cell flow pattern: (a) contour plot of u; (b) vector plot of (v, w)

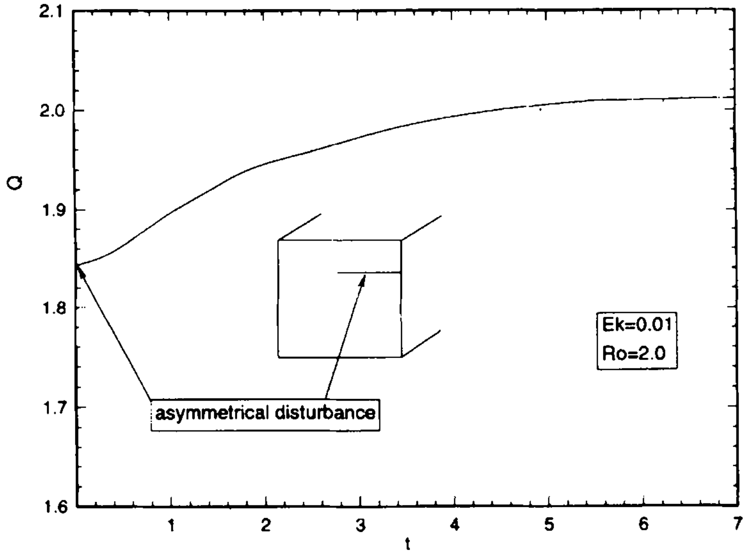

Figure 17. Flow rate versus time with as

continues to attract the small cell (Figure 18(c)). Eventually the bottom big cell pushes the merged big cell to its original location and the flow pattern becomes a two-cell flow pattern (Figure 18(d)). Thus the four-cell flow pattern under asymmetrical disturbances does not go back to its original state. Instead it developes into the two-cell flow pattern. By the definition of hydrodynamic instability mentioned above, the four-cell flow pattern is unstable to asymmetrical disturbances. The present numerical simulation confirms the recent bifurcation study results.

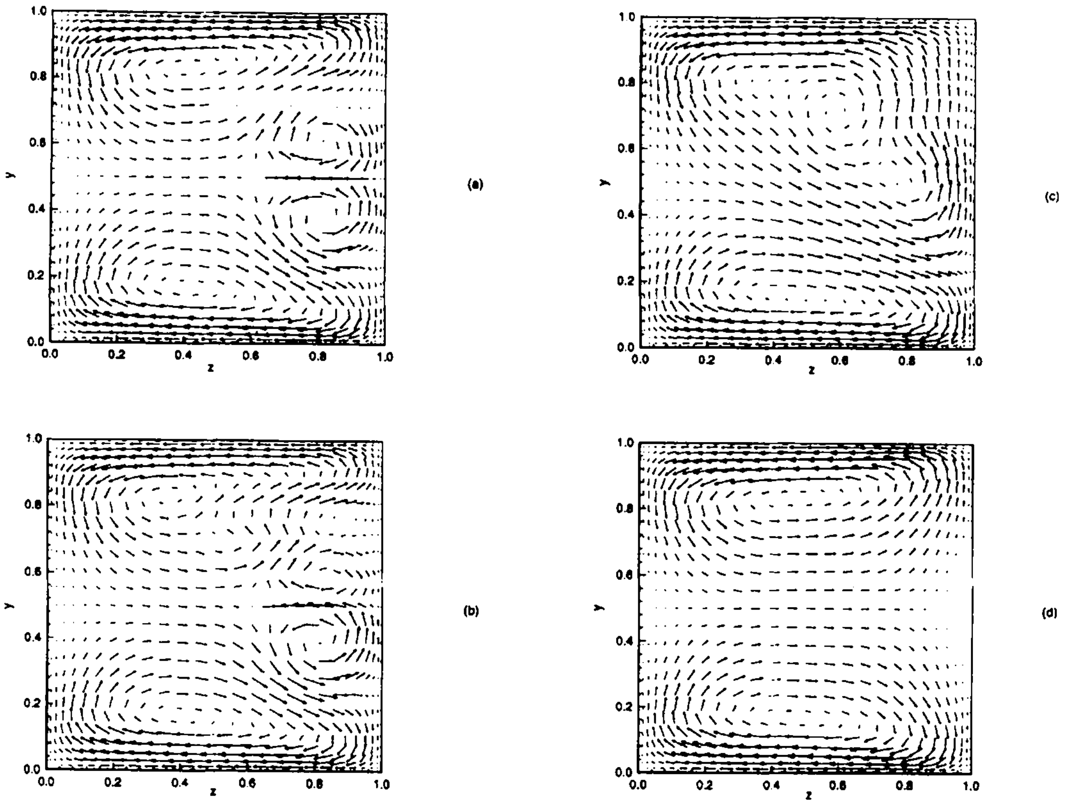

Figure 18. Vector plot of (v, w) with asymmetrical disturbances ($Ek = 0{\cdot}01$, $Ro = 2$): (a) $t = 0$; (b) $t = 0{\cdot}05$; (c) $t = 0{\cdot}55$; (d) $t = 5{\cdot}55$

5. CONCLUSION

We have presented a Fourier–Chebyshev pseudospectral matrix method for the numerical simulation of incompressible flows in a three-dimensional channel flow with rotation. Realistic, non-periodic boundary conditions in two directions (spanwise and vertical directions) are used with this new approach. The Navier–Stokes equations are integrated in time using a fractional step method. The Poisson equation for pressure and the Helmholtz equation for velocity are solved using a matrix diagonalization (eigenfunction decomposition) method, through which we are able to reduce a 3D matrix probem to a simple algebraic vector equation. This is a great advantage in terms of computer storage for large-scale computations. Verification of the code is conducted by duplicating an exact rectilinear channel flow and the rotating 2D case. Two-cell flow patterns are found at $Ek = 0{\cdot}01$ and $Ro = 0$, $Ro = 1$. It is observed in our numerical simulation that the two-cell flow pattern spontaneously develops into the four-cell flow pattern at $Ek = 0{\cdot}01$ and $Ro = 2$. Morever, it is concluded that the four-cell flow pattern is stable to symmetrical disturbances but unstable to asymmetrical disturbances. The next step will be to examine the breakdown of the two-dimensional flows into three-dimensional ones at higher Rossby numbers

ACKNOWLEDGEMENTS

H.B.C. would like to thank Dr. J. Chen of Eaton Semiconductor Corporation for reading the manuscript and for useful comments. W.H.F., K.N. and H.B.C. gratefully acknowledge the funding of NSERC.

REFERENCES

1. H. S. Kheshgi and L. E. Scriven, 'Viscous flow through a rotating square channel', *Phys. Fluids*, **28**, 2868–2979 (1985).
2. K. Nandakumar, H. Raszillier and F. Durst, 'Flow through rotating rectangular ducts', *Phys. Fluids A*, **3**, 770–781 (1991).
3. W. H. Finlay, 'Transition to oscillatory motion in rotating channel flow', *J. Fluid Mech.*, **194**, 209–227 (1990).
4. C. Canuto, M. Y. Hussaini, A. Quarteroni and T. A. Zang, *Spectral Methods in Fluids Dynamics*, Springer, New York, 1988.
5. H. B. Chen, W. H. Finlay, K. Nandakumar and H. C. Ku, 'Solution of 3-D Navier–Stokes equations: a pseudospectral matrix method approach', *Proc. Conf. of Computational Fluid Dynamics Society of Canada*, Montreal, 1993, pp. 151–161.
6. H. B. Chen, 'On the instability of non-parallel flow: Kovasznay flow', *Int. j. numer. Methods Fluids*, **17**, 731–754 (1993).
7. H. C. Ku, R. S. Hirsch and T. D. Taylor, 'A pseudospectral method for solution of the three-dimensional incompressible Navier–Stokes equations', *J. Comput. Phys.*, **70**, 549–462 (1987).
8. D. B. Haidvogel and T. A. Zang, 'The accurate solution of Poisson's equation by expansion in Chebyshev polynomials', *J. Comput. Phys.*, **30**, 167–180 (1979).
9. C. A. J. Fletcher, *Computational Techniques for Fluid Dynamics*, Vols 1 and 2, Springer, New York, 1988.
10. C. G. Spezial and T. Sivagnanam, 'Numerical study of secondary flows and roll-cell instabilities in rotating channel flow', *J. Fluid Mech.*, **130**, 337–355 (1983).